
This is an electronic reprint of the original article.
This reprint may differ from the original in pagination and typographic detail.

Lamberg, Joel; Lamberg, Lasse; Tamminen, Aleks; Ala-Laurinaho, Juha; Taylor, Zachary
Extended legality of curved boundary integral method

Published in:
Optics Express

DOI:
[10.1364/OE.524189](https://doi.org/10.1364/OE.524189)

Published: 29/07/2024

Document Version
Publisher's PDF, also known as Version of record

Published under the following license:
Unspecified

Please cite the original version:
Lamberg, J., Lamberg, L., Tamminen, A., Ala-Laurinaho, J., & Taylor, Z. (2024). Extended legality of curved boundary integral method. *Optics Express*, 32(16), 28231-28244. <https://doi.org/10.1364/OE.524189>

This material is protected by copyright and other intellectual property rights, and duplication or sale of all or part of any of the repository collections is not permitted, except that material may be duplicated by you for your research use or educational purposes in electronic or print form. You must obtain permission for any other use. Electronic or print copies may not be offered, whether for sale or otherwise to anyone who is not an authorised user.



Extended legality of curved boundary integral method

JOEL LAMBERG,^{1,*}  LASSE LAMBERG,² ALEKSI TAMMINEN,¹ JUHA ALA-LAURINAHO,¹ AND ZACHARY TAYLOR¹ 

¹*Department of Electronics and Nanotechnology, Aalto University, Finland*

²*Department of Mathematics and Statistics, University of Helsinki, Finland*

*joel.lamberg@aalto.fi

Abstract: The angular spectrum method is an efficient approach for synthesizing electromagnetic beams from planar electric field distributions. The electric field definition is restricted to a plane, which can introduce inaccuracy when applying the synthesized beam to curved surface features. The angular spectrum method can also be interpreted as a pure source method defining the field symmetrically with respect to the creation plane. Recently, we generalized that symmetric field method to arbitrary source distributions, which are valid at any point on compact, regular surface Ω in \mathbb{R}^3 . We call this approach the Curved Boundary Integral method. The electromagnetic fields synthesized with this method satisfy the Helmholtz equation and are adjusted via amplitude and phase at the desired surface. The fields are obtained as a relatively simple integral. However, restrictions on where in space the synthesized field is valid were included in the mathematical proof length to avoid obscuring the main points. These restrictions can be significant depending on the shape and degree of curvature of surface Ω . In this article, we remove these restrictions so that the integral representation of the electromagnetic beam becomes valid at all points $\mathbf{r} \in \mathbb{R}^3 \setminus \Omega$, with a minor restriction. Its modification can work even on Ω . We demonstrate the importance of this extended legality with a source field parametrized into the torus surface. The electromagnetic radiation of this structure would not be valid at any point in space without this extension. Finally, we show that by changing the order of integration, the field singularity at each source point is eliminated.

© 2024 Optica Publishing Group under the terms of the [Optica Open Access Publishing Agreement](#)

1. Introduction

The Angular Spectrum Method (ASM) is a rigorous method to synthesize near and far-field electromagnetic (EM) and acoustic fields from known planar field distribution. ASM provides a robust framework for examining wave propagation in various scenarios by decomposing the fields into constituent plane waves [1–10]. In previously published work, we expanded planar symmetric ASM theory to the curved boundary integral method (CBIM), to synthesize electromagnetic fields from arbitrary surface electric field distributions positioned inside/outside of the computational domain or even on the sub-region of a scatterer's surface [11]. CBIM allows for greater flexibility in beam design as it enables sources to be freely placed within the computational domain. It also allows for analyzing electromagnetic forward/backward propagation between optical elements using a single method. In separate articles, we also derive a 3D angular spectrum method from CBIM to obtain beam shape coefficients for the spherical harmonics presentation used to compute Mie scattering from homogeneous and layered spherical targets. [12,13].

In previous work [11], we presented a mathematical proof for the CBIM summarized in Eq. (1–4) in this article, with a limitation: the electromagnetic field radiated from each source point on the surface distribution is not defined on a source point's tangential plane on the surface. This condition is presented in Eq. (5).

This article clarifies that the total electromagnetic field synthesized by the CBIM is a coherent superposition of fields emanating from individual source points. Our addresses a key insight: if

the field from even a single source point is undefined, it compromises the validity of the entire synthesized field. By removing the restriction outlined in Eq. (5), we demonstrate that the fields remain well-defined at each source point and its corresponding plane, ensuring the integrity of the overall electromagnetic field representation. Further, a change in the integration order of the field presentation eliminates singularities exactly at the source point.

2. Restrictions mathematical definition

Source point's restriction on its tangential plane is presented mathematically as follows. Let $\Psi = \{(p, q)\}$ be a compact set in \mathbb{R}^2 and let $\mathbf{o} : \Psi \rightarrow \mathbb{R}^3$ be a continuously differentiable function. The mapping \mathbf{o} defines a compact, regular surface $\Omega = \{\mathbf{o}(p, q) | (p, q) \in \Psi\}$ in \mathbb{R}^3 and a tangent plane and normal to each of its points $\mathbf{o}(p, q)$. Keeping each \mathbf{o} as a local origin, unit vectors $(\mathbf{e}_1, \mathbf{e}_2, \mathbf{e}_3)$ define a base for the local orthonormal coordinates, where \mathbf{e}_1 and \mathbf{e}_2 lie in the tangent plane, and \mathbf{e}_3 is along the surface normal, see Fig. 1.

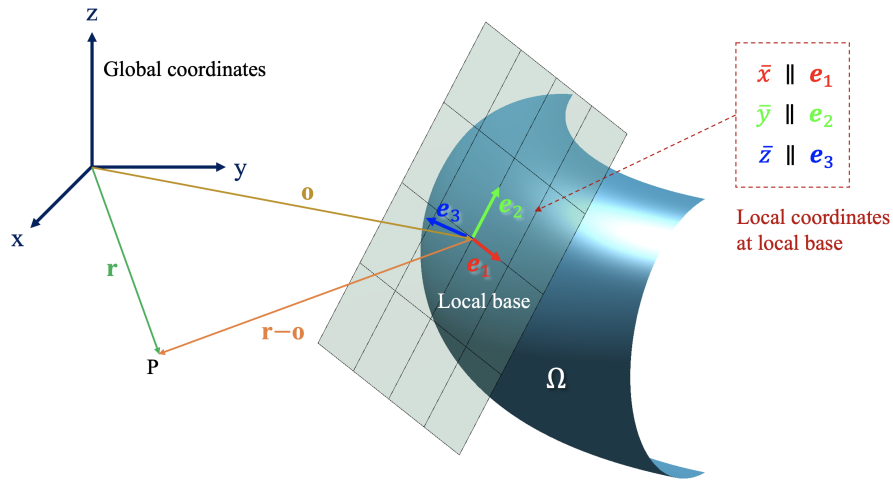


Fig. 1. Relation between global and local coordinate systems of a source point at $\mathbf{o} \in \Omega$. Also, local base vectors \mathbf{e}_1 and \mathbf{e}_2 span a tangential plane, where radiated electric and magnetic fields are not valid without the proofs of this article.

Let E_0 be a continuous electric field defined on the surface Ω . At the limit, using the analysis in [11], we end up with the fact that each electric field at a point \mathbf{o} on the surface Ω creates propagating electric and magnetic field densities. Without loss of generality, the electric field is chosen to be polarized at the local $(\mathbf{e}_1, \mathbf{e}_3)$ -plane as

$$\begin{aligned} \mathbf{E}(\mathbf{r}; \mathbf{o}) &= E_0(E_1\mathbf{e}_1 + E_3\mathbf{e}_3), \\ \mathbf{H}(\mathbf{r}; \mathbf{o}) &= E_0(H_1\mathbf{e}_1 + H_2\mathbf{e}_2 + H_3\mathbf{e}_3), \end{aligned} \tag{1}$$

where \mathbf{r} is the position vector of observation point P in the global coordinate system, see Fig. 1, and the magnetic field is obtained as a curl of the electric field. The local field E_1 is cylindrically symmetric and oriented along the source point's tangential plane. The local field E_3 is normal to the source point's tangential plane and cylindrically asymmetrical due to the term k_x/k_z . These fields are obtained as

$$\begin{aligned} E_1 &= \frac{1}{4\pi^2} \iint_{-\infty}^{\infty} e^{i(k_x x + k_y y)} f(r; |z|) dk_x dk_y = \frac{1}{4\pi^2} \int_0^{\infty} f(r; |z|) J_0(sr) r dr, \\ E_3 &= -\frac{\text{sign}(z)}{4\pi^2} \iint_{-\infty}^{\infty} e^{i(k_x x + k_y y)} \frac{k_x}{\sqrt{k^2 - k_x^2 - k_y^2}} f(r; |z|) dk_x dk_y, \end{aligned} \tag{2}$$

where k is a constant, x, y and z are local coordinates of $\mathbf{r} - \mathbf{o}$, that is, they present the position of P in the local coordinate system related to \mathbf{o} [11–13], $r^2 = k_x^2 + k_y^2$, $s^2 = x^2 + y^2$, and J_0 is the zero-order Bessel function and

$$f(k_x, k_y; |z|) = f(r; |z|) = e^{i|z|\sqrt{k^2 - k_x^2 - k_y^2}}. \quad (3)$$

The Fourier transform for a cylindrically symmetric function is obtained via the zero-order Bessel function. Here, we use it in the presentation of E_1 and later in Eq. (8) [14]. This observation is crucial in estimating the difference $E_1 - D$, where D will be defined in Eq. (8). The total electric and magnetic fields are obtained as surface integrals

$$\begin{aligned} \mathbf{E}(\mathbf{r}) &= \iint_{\Omega} E_0(\mathbf{o}) \left[E_1(\mathbf{r}; \mathbf{o}) \mathbf{e}_1(\mathbf{o}) + E_3(\mathbf{r}; \mathbf{o}) \mathbf{e}_3(\mathbf{o}) \right] d\Omega, \\ \mathbf{H}(\mathbf{r}) &= \iint_{\Omega} E_0(\mathbf{o}) \left[H_1(\mathbf{r}; \mathbf{o}) \mathbf{e}_1(\mathbf{o}) + H_2(\mathbf{r}; \mathbf{o}) \mathbf{e}_2(\mathbf{o}) + H_3(\mathbf{r}; \mathbf{o}) \mathbf{e}_3(\mathbf{o}) \right] d\Omega, \end{aligned} \quad (4)$$

where $d\Omega = \|\frac{\partial \mathbf{o}}{\partial p} \times \frac{\partial \mathbf{o}}{\partial q}\| dpdq$. We proved in [11] that expressions in Eq. (4) are valid at the point \mathbf{r} , where $z \neq 0$ in every local coordinate system, which can be written more precisely

$$\Omega_0(\mathbf{r}) = \left\{ \mathbf{o} \in \Omega \mid z(\mathbf{r}; \mathbf{o}) = (\mathbf{r} - \mathbf{o}) \cdot \left(\frac{\partial \mathbf{o}}{\partial p} \times \frac{\partial \mathbf{o}}{\partial q} \right) = 0 \right\} = \emptyset. \quad (5)$$

This assumption we designate as $AS(\mathbf{r})$. When $z = 0$, the integrals in Eq. (2) do not exist in the usual sense. This article eliminates the presented limitation Eq. (5), in which the effect strongly depends on the shape of the surface Ω . For example, a surface can be easily found where the assumption in Eq. (5) is not satisfied for any $\mathbf{r} \in \mathbb{R}^3$, then Eq. (4) would not be defined at any point \mathbf{r} , see Fig. 2.

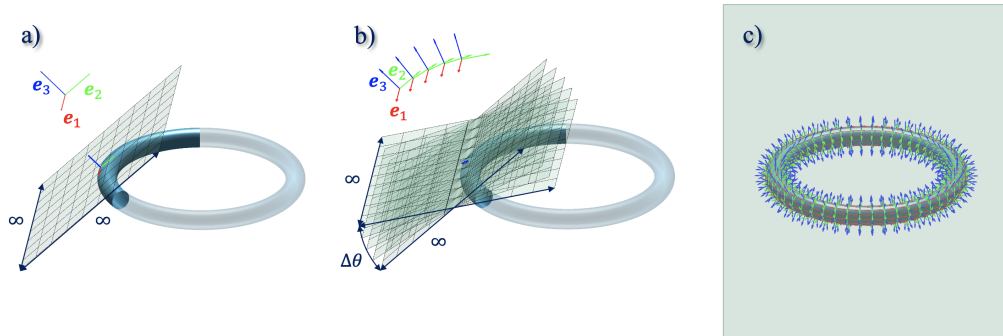


Fig. 2. Limitation for $\mathbf{E}(\mathbf{r})$ and $\mathbf{H}(\mathbf{r})$ fields when assumption $AS(\mathbf{r})$ is not valid. a) A single source point spans a tangential plane where $AS(\mathbf{r})$ is not valid. b) A surface line of source points spans a space of tangential planes where $AS(\mathbf{r})$ is not valid. c) The whole torus is discretized to source points, whose tangential planes span the whole \mathbb{R}^3 space where $AS(\mathbf{r})$ is not valid.

It was proved in [11] that once $z \neq 0$, the corresponding $\mathbf{E}(\mathbf{r}; \mathbf{o})$ and $\mathbf{H}(\mathbf{r}; \mathbf{o})$ exist. Next in this article, we will show that $\lim_{z \rightarrow 0^+} \mathbf{E}(\mathbf{r}; \mathbf{o})$ and $\lim_{z \rightarrow 0^-} \mathbf{E}(\mathbf{r}; \mathbf{o})$, as well as, $\lim_{z \rightarrow 0^+} \mathbf{H}(\mathbf{r}; \mathbf{o})$ and $\lim_{z \rightarrow 0^-} \mathbf{H}(\mathbf{r}; \mathbf{o})$ always exist, when $\mathbf{r} \in \mathbb{R}^3 \setminus \Omega$. This helps us to define the fields $\mathbf{E}(\mathbf{r})$ and $\mathbf{H}(\mathbf{r})$ at every point $\mathbf{r} \in \mathbb{R}^3 \setminus \Omega$.

3. Validity of curved boundary integral method

In this section, we show that the electric and magnetic field presentation is valid at points \mathbf{r} , where assumption $AS(\mathbf{r})$, illustrated in Fig. 2, is not. The main results are the E-field proof in

Theorem 3.3 and its H-field analogue in Theorem 3.5. First, we prove the existence of limits for E_3 and E_1 components when the local coordinate $z \rightarrow 0$, followed by the magnetic field components H_1, H_2 , and H_3 .

3.1. Electric field E_3 component

Let's define for $\mathbf{r} \in \mathbb{R}^3 \setminus \Omega$

$$\begin{aligned} \Omega_+(\mathbf{r}) &= \left\{ \mathbf{o} \in \Omega \mid (\mathbf{r} - \mathbf{o}) \cdot \left(\frac{\partial \mathbf{o}}{\partial p} \times \frac{\partial \mathbf{o}}{\partial q} \right) \geq 0 \right\}, \\ \Omega_-(\mathbf{r}) &= \left\{ \mathbf{o} \in \Omega \mid (\mathbf{r} - \mathbf{o}) \cdot \left(\frac{\partial \mathbf{o}}{\partial p} \times \frac{\partial \mathbf{o}}{\partial q} \right) \leq 0 \right\}. \end{aligned} \tag{6}$$

Note that $\Omega_0(\mathbf{r}) = \Omega_+(\mathbf{r}) \cap \Omega_-(\mathbf{r})$.

Lemma 3.1. *Let Ω be a regular, compact surface in \mathbb{R}^3 , especially $\frac{\partial \mathbf{o}}{\partial p} \times \frac{\partial \mathbf{o}}{\partial q} \neq \mathbf{0}$ for all $\mathbf{o} \in \Omega$. There exist $\lim_{z \rightarrow 0^+} E_3$ and $\lim_{z \rightarrow 0^-} E_3 = -\lim_{z \rightarrow 0^+} E_3$ at $(\mathbf{r}, \mathbf{o}) \in (\mathbb{R}^3 \setminus \Omega) \times \Omega_0(\mathbf{r})$. The function E_3 extended by the former limit depends continuously on (\mathbf{r}, \mathbf{o}) in the product set $(\mathbb{R}^3 \setminus \Omega) \times \Omega_+(\mathbf{r})$. Correspondingly, E_3 extended by the latter limit depends continuously on (\mathbf{r}, \mathbf{o}) in the $(\mathbb{R}^3 \setminus \Omega) \times \Omega_-(\mathbf{r})$.*

Proof. Denote

$$g(k_x, k_y; |z|) = g(r; |z|) = e^{-|z|\sqrt{k_x^2+k_y^2}} = e^{-|z|r}. \tag{7}$$

We compare the integrals in Eq. (2) with the integral obtained when f in E_1 is replaced by g . The reason is that the plane's Fourier transform of g is known when the constant $z \neq 0$ [15]. Thus we obtain

$$\begin{aligned} D &= \mathfrak{F}^{-1} \{g(k_x, k_y; |z|)\} (x, y) = \frac{1}{4\pi^2} \iint_{-\infty}^{\infty} e^{i(xk_x+yk_y)} g(k_x, k_y; |z|) dk_x dk_y \\ &= \frac{1}{4\pi^2} \int_0^{\infty} g(r; |z|) J_0(sr) r dr = \frac{C_2 |z|}{(|z|^2 + s^2)^{3/2}}, \end{aligned} \tag{8}$$

where C_2 is a constant. When $z \neq 0$, according to Eq. (2) and Eq. (3) we obtain a source-free electric field, equivalent to $\nabla \cdot \mathbf{E} = 0$, as

$$\frac{\partial E_3}{\partial z} = \frac{-i}{4\pi^2} \iint_{-\infty}^{\infty} e^{i(xk_x+yk_y)} k_x f(r; |z|) dk_x dk_y = -\frac{\partial E_1}{\partial x}. \tag{9}$$

Assume $\mathbf{r} \in \mathbb{R}^3 \setminus \Omega$ and its z-coordinate is zero in a local coordinate system related to $\mathbf{o} \in \Omega$. Then definitely $s = \sqrt{x^2 + y^2} \neq 0$ in this local system, which we fix. We approach r along the line $\{(x, y, z) \mid z \neq 0\}$ retaining these x and y , and letting z go to zero. Equations Eq. (2) and Eq. (3) are valid at this kind of point. See Figure (3).

We will show that Eq. (9) goes to zero when z does it; in that case, the standard analysis shows that there exist one-side limits $\lim_{z \rightarrow 0^+} E_3$ and $\lim_{z \rightarrow 0^-} E_3$, for which it would be sufficient that the derivative $\frac{\partial E_3}{\partial z}$ remains bounded.

Consider the representation $E_1 = E_1 - D + D$ and its derivative $\frac{\partial}{\partial x}$. Based on Eq. (8), we obtain

$$\frac{\partial D}{\partial x} = -\frac{3C_2 |z| x}{(|z|^2 + s^2)^{5/2}} \rightarrow 0, \quad \text{when } z \rightarrow 0, \tag{10}$$

even uniformly in a compact set where $s \neq 0$. When $r \geq k$, it follows

$$f(r; |z|) = e^{i|z|\sqrt{r^2-k^2}} \geq g(r; |z|). \tag{11}$$

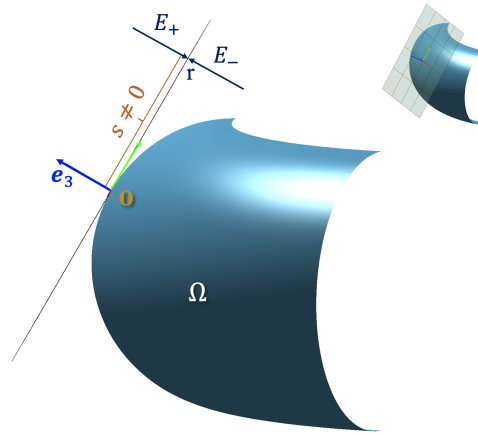


Fig. 3. Illustration of source point’s tangential plane, where we will prove the legality of $\mathbf{E}(\mathbf{r}; \mathbf{o})$ and $\mathbf{H}(\mathbf{r}; \mathbf{o})$ when $s \neq 0$.

Let’s fix $r_0 > k$. Then we obtain

$$E_1 - D = \frac{1}{4\pi^2} \int_0^{r_0} [f(r; |z|) - g(r; |z|)] J_0(sr) r dr + \frac{1}{4\pi^2} \int_{r_0}^{\infty} [f(r; |z|) - g(r; |z|)] J_0(sr) r dr, \tag{12}$$

where the derivative $\frac{\partial}{\partial x}$ of the first integral, $\frac{1}{4\pi^2} \int_0^{r_0} [f(r; |z|) - g(r; |z|)] J_0(sr) r dr$, clearly goes to zero as $z \rightarrow 0$, since $(f - g) \rightarrow 0$ uniformly.

It is sufficient to consider only the derivative of the latter integral. When $k < r_0 \leq r$, based on Taylor series

$$f(r; |z|) - g(r; |z|) = e^{-|z|r} \left[e^{|z|(r - \sqrt{r^2 - k^2})} - 1 \right] = e^{-|z|r} \left[e^{\frac{|z|k^2}{r + \sqrt{r^2 - k^2}}} - 1 \right] = e^{-|z|r} \left\{ \frac{|z|k^2}{r + \sqrt{r^2 - k^2}} \left[1 + \frac{1}{2!} \frac{|z|k^2}{r + \sqrt{r^2 - k^2}} + \frac{1}{3!} \left(\frac{|z|k^2}{r + \sqrt{r^2 - k^2}} \right)^2 + \dots \right] \right\}. \tag{13}$$

This follows

$$[f(r; |z|) - g(r; |z|)] r = |z|k^2 e^{-|z|r} \left\{ \frac{r}{r + \sqrt{r^2 - k^2}} \left[1 + \frac{1}{2!} \frac{|z|k^2}{r + \sqrt{r^2 - k^2}} + \dots \right] \right\} =: |z|k^2 e^{-|z|r} h(r; |z|). \tag{14}$$

It is straightforward to show that the functions $h(r; |z|)$ and $\left[\frac{\partial}{\partial r} h(r; |z|) \right] r$ are bounded functions in the set $r \in [r_0, \infty[$, $|z| < 1$; the derivation in the series in Eq. (13) and Eq. (14) can be done term by term using the power series derivation rule. Thus, we find the constants $K_1, K_2 > 0$ such that

$$|h(r; |z|)| \leq K_1 \quad \text{and} \quad \left| \frac{\partial}{\partial r} [h(r; |z|)r] \right| \leq K_2, \quad \text{with all } r \in [r_0, \infty[\text{ and } |z| < 1. \tag{15}$$

By partial integration and from Eq. (14) we obtain

$$\begin{aligned} & \frac{\partial}{\partial x} \left\{ \frac{1}{4\pi^2} \int_{r_0}^{\infty} [f(r; |z|) - g(r; |z|)] J_0(sr) r dr \right\} \\ &= \frac{|z|k^2 x}{4\pi^2 s} \int_{r_0}^{\infty} e^{-|z|r} h(r; |z|) r J_0'(sr) dr = \frac{|z|k^2 x}{4\pi^2 s^2} \left\{ \int_{r_0}^{\infty} e^{-|z|r} h(r; |z|) r J_0(sr) \right. \\ &+ |z| \int_{r_0}^{\infty} e^{-|z|r} h(r; |z|) r J_0(sr) dr - \int_{r_0}^{\infty} e^{-|z|r} \frac{\partial}{\partial r} [h(r; |z|) r] J_0(sr) dr \left. \right\} \\ &= \frac{|z|k^2 x}{4\pi^2 s^2} \left\{ -e^{-|z|r_0} h(r_0; |z|) r_0 J_0(sr_0) + |z| \int_{r_0}^{\infty} \dots - \int_{r_0}^{\infty} \dots \right\}. \end{aligned} \tag{16}$$

Next, we use an asymptotic estimate that holds for the Bessel function as [16]

$$J_0(v) = \sqrt{\frac{2}{\pi v}} \cos\left(v - \frac{\pi}{4}\right) + O(|v|^{-1}). \tag{17}$$

As a result, for some $a > 0$ it holds

$$|J_0(v)| \leq a|v|^{-1/2} \text{ with all } v. \tag{18}$$

Based on this and Eq. (15), we obtain from Eq. (16)

$$\begin{aligned} & \left| \frac{\partial}{\partial x} \left\{ \frac{1}{4\pi^2} \int_{r_0}^{\infty} [f(r; |z|) - g(r; |z|)] J_0(sr) r dr \right\} \right| \\ & \leq \frac{|x||z|k^2}{4\pi^2 s^2} \left\{ e^{-|z|r_0} K_1 r_0 a s^{-1/2} r_0^{-1/2} + |z| \int_{r_0}^{\infty} e^{-|z|r} r K_1 a s^{-1/2} r^{-1/2} dr \right. \\ & \left. + \int_{r_0}^{\infty} e^{-|z|r} K_2 a s^{-1/2} r^{-1/2} dr \right\}. \end{aligned} \tag{19}$$

Let us substitute the variables $t = |z|r \rightarrow r = t/|z|$ and $dr = dt/|z|$ in the Eq. (19) and show that it goes to zero as

$$\begin{aligned} & \frac{A|z|}{s^2} \left\{ e^{-|z|r_0} r_0^{1/2} s^{-1/2} K_1 + \frac{|z|K_1}{s^{1/2}} \int_{|z|r_0}^{\infty} e^{-t} \left(\frac{t}{|z|}\right)^{1/2} \frac{dt}{|z|} + \frac{K_2}{s^{1/2}} \int_{|z|r_0}^{\infty} e^{-t} \left(\frac{|z|}{t}\right)^{1/2} \frac{dt}{|z|} \right\} \\ & \leq \frac{A|z|^{1/2}}{s^{5/2}} \left\{ e^{-|z|r_0} |z|^{1/2} r_0^{1/2} K_1 + K_1 \int_0^{\infty} e^{-t} t^{1/2} dt + K_2 \int_0^{\infty} e^{-t} t^{-1/2} dt \right\} \\ & \leq \frac{A|z|^{1/2}}{s^{5/2}} \left\{ e^{-|z|r_0} |z|^{1/2} r_0^{1/2} K_1 + (K_1 + 2K_2) \int_0^{\infty} e^{-t} t^{1/2} dt \right\} \rightarrow 0, \text{ when } z \rightarrow 0, \end{aligned} \tag{20}$$

where $A = \frac{ak^2|x|}{4\pi^2}$. Thus, by Eq. (9), Eq. (10) and Eq. (20) we obtain

$$-\frac{\partial E_3}{\partial z} = \frac{\partial E_1}{\partial x} = \frac{\partial}{\partial x}(E_1 - D) + \frac{\partial D}{\partial x} \rightarrow 0, \text{ when } z \rightarrow 0, \tag{21}$$

even uniformly in a closed set of s where $s \neq 0$. Examining the standard Cauchy sequences using the mean value theorem shows that there exists $\lim_{z \rightarrow 0^+} E_3$ and $\lim_{z \rightarrow 0^-} E_3$ when $(\mathbf{r}, \mathbf{o}) \in (\mathbb{R}^3 \setminus \Omega) \times \Omega_0(\mathbf{r})$. Additionally, E_3 changes its sign concomitantly with z . Thus $\lim_{z \rightarrow 0^-} E_3 = -\lim_{z \rightarrow 0^+} E_3$.

Let's denote $E_3^+(\mathbf{r}, \mathbf{o})$ and $E_3^-(\mathbf{r}, \mathbf{o})$ as extensions of $E_3(\mathbf{r}, \mathbf{o})$ by $\lim_{z \rightarrow 0^+} E_3$ and $\lim_{z \rightarrow 0^-} E_3$ onto the set $(\mathbb{R}^3 \setminus \Omega) \times \Omega_+(\mathbf{r})$ and $(\mathbb{R}^3 \setminus \Omega) \times \Omega_-(\mathbf{r})$, respectively. Their continuity follows from uniform convergence.

3.2. Electric field E_1 component

Lemma 3.2. Let Ω be a regular, compact surface in \mathbb{R}^3 , especially $\frac{\partial \mathbf{o}}{\partial p} \times \frac{\partial \mathbf{o}}{\partial q} \neq \mathbf{0}$ for all $\mathbf{o} \in \Omega$.

There exist $E_1(x, y, z) \rightarrow 0$ uniformly in set $s = \sqrt{x^2 + y^2} \in [\nu, \infty[$ with all $\nu > 0$ when $z \rightarrow 0$.

Proof. Let us examine the representation $E_1 = E_1 - D + D$ again. Based on Eq. (8), $D \rightarrow 0$ uniformly in relation to constant s in the set $[\nu, \infty[$, when $z \rightarrow 0$. Let us fix $r_0 > k$. Again, in the difference $E_1 - D = \frac{1}{4\pi^2} \int_0^\infty [f(r; |z|) - g(r; |z|)] J_0(sr) r dr$ it is sufficient to examine the integral

$$I = \frac{1}{4\pi^2} \int_{r_0}^\infty [f(r; |z|) - g(r; |z|)] J_0(sr) r dr, \tag{22}$$

where by Eq. (14) we obtain $[f(r; |z|) - g(r; |z|)] r = |z| k^2 e^{-|z|r} h(r; |z|)$. Based on Eq. (15) and Eq. (19), we obtain as in Eq. (20)

$$\begin{aligned} |I| &\leq \frac{|z| k^2}{4\pi^2} \int_{r_0}^\infty e^{-|z|r} |h(r; |z|)| |J_0(sr)| dr \leq \dots \\ &\leq |z|^{1/2} \frac{ak^2 K_1}{2\pi^2 s^{1/2}} \int_0^\infty e^{-t} t^{1/2} dt \rightarrow 0, \text{ when } z \rightarrow 0, \end{aligned} \tag{23}$$

even uniformly in the set $s \in [\nu, \infty[$, $\nu > 0$.

NOTE. When considering Eq. (12), because of Eq. (8) and $|J_0(sr)| \leq as^{-1/2} r^{-1/2}$, it is also shown that for all $z \neq 0$ holds $E_1(x, y, |z|) \rightarrow 0$ at least at a rate $s^{-1/2}$ when $s \rightarrow \infty$.

3.3. Theorem for the electric field

Theorem 3.3. Let Ω be a regular, compact surface in \mathbb{R}^3 , especially $\frac{\partial \mathbf{o}}{\partial p} \times \frac{\partial \mathbf{o}}{\partial q} \neq \mathbf{0}$ for all $\mathbf{o} \in \Omega$.

The electric field E_0 on the surface Ω creates a radiating field $\mathbf{E}(\mathbf{r})$ with the representation in Eq. (4) at the point $\mathbf{r} \in \mathbb{R}^3 \setminus \Omega$, where the set $\Omega_0(\mathbf{r})$ is of measure zero in $d\Omega$. Moreover, $\mathbf{E}(\mathbf{r})$ is a continuous function of \mathbf{r} at those points.

Proof. Let $\mathbf{r} \in \mathbb{R}^3 \setminus \Omega$. When $z = 0$, let us define $E_1(x, y, 0) = \lim_{z \rightarrow 0} E_1$. Then the functions

$$\begin{aligned} \mathbf{E}^+(\mathbf{r}; \mathbf{o}) &= E_0[E_1(\mathbf{r}; \mathbf{o})\mathbf{e}_1 + E_3^+(\mathbf{r}; \mathbf{o})\mathbf{e}_3], \\ \mathbf{E}^-(\mathbf{r}; \mathbf{o}) &= E_0[E_1(\mathbf{r}; \mathbf{o})\mathbf{e}_1 + E_3^-(\mathbf{r}; \mathbf{o})\mathbf{e}_3] \end{aligned} \tag{24}$$

are continuous in $(\mathbb{R}^3 \setminus \Omega) \times \Omega_+(\mathbf{r})$ and $(\mathbb{R}^3 \setminus \Omega) \times \Omega_-(\mathbf{r})$, respectively. In what follows in the proof, let $\mathbf{r} \in \mathbb{R}^3 \setminus \Omega$ be such that the corresponding $\Omega_0(\mathbf{r})$ is of measure zero in $d\Omega$. Then integral in Eq. (4) exists as

$$\mathbf{E}(\mathbf{r}) = \iint_{\Omega_+(\mathbf{r})} \mathbf{E}^+(\mathbf{r}; \mathbf{o}) d\Omega + \iint_{\Omega_-(\mathbf{r})} \mathbf{E}^-(\mathbf{r}; \mathbf{o}) d\Omega. \tag{25}$$

By continuity, we can expect that $\Omega_0(\mathbf{r}) \neq \emptyset$. Let us define $\varepsilon, \nu > 0$ and $\Omega_\nu(\mathbf{r}) = \{\mathbf{o} \in \Omega \mid d(\mathbf{o}, \Omega_0(\mathbf{r})) < \nu\}$. It follows from continuity in a compact set that there exists some $\delta_\nu > 0$ such that

$$\Omega_0(\mathbf{s}) \subset \Omega_\nu(\mathbf{r}) \text{ for all } \mathbf{s} \in B(\mathbf{r}, \delta_\nu), \tag{26}$$

where $B(\mathbf{r}, \delta_\nu)$ is an open ball. Also, by continuity the jump $\|\mathbf{E}^\pm(\mathbf{r}; \mathbf{o}) - \mathbf{E}^\pm(\mathbf{s}; \mathbf{o})\|$ in a compact set $\bar{B}(\mathbf{r}, \delta_\nu) \times \bar{\Omega}_\nu(\mathbf{r})$ is bounded by some $M > 0$. Then for all $\mathbf{s} \in B(\mathbf{r}, \delta_\nu)$ it holds that

$$\iint_{\bar{\Omega}_\nu(\mathbf{r})} \|\mathbf{E}^\pm(\mathbf{r}; \mathbf{o}) - \mathbf{E}^\pm(\mathbf{s}; \mathbf{o})\| d\Omega < M \iint_{\bar{\Omega}_\nu(\mathbf{r})} d\Omega. \tag{27}$$

But $\cap_{\nu > 0} \bar{\Omega}_\nu(\mathbf{r}) = \Omega_0(\mathbf{r})$, and hence

$$\iint_{\bar{\Omega}_\nu(\mathbf{r})} d\Omega \rightarrow \iint_{\Omega_0(\mathbf{r})} d\Omega = 0 \text{ when } \nu \rightarrow 0. \tag{28}$$

For all $\mathbf{s} \in B(\mathbf{r}, \delta_\nu)$ we can find $\nu > 0$ satisfying Eq. (26) such that the value of the integral in Eq. (27) is less than $\varepsilon/2$. Let $|\Omega|$ be a measure of Ω . Moreover, because of continuity, we can reduce δ_ν such that

$$\|\mathbf{E}(\mathbf{r}; \mathbf{o}) - \mathbf{E}(\mathbf{s}; \mathbf{o})\| < \frac{\varepsilon}{2|\Omega|} \text{ for all } (\mathbf{s}, \mathbf{o}) \in B(\mathbf{r}, \delta_\nu) \times \Omega \setminus \Omega_\nu(\mathbf{r}). \tag{29}$$

As a consequence, we get that

$$\begin{aligned} \|\mathbf{E}(\mathbf{r}) - \mathbf{E}(\mathbf{s})\| &\leq \iint_{\bar{\Omega}_\nu(\mathbf{r})} \|\mathbf{E}^\pm(\mathbf{r}; \mathbf{o}) - \mathbf{E}^\pm(\mathbf{s}; \mathbf{o})\| d\Omega \\ &\quad + \iint_{\Omega \setminus \bar{\Omega}_\nu(\mathbf{r})} \|\mathbf{E}(\mathbf{r}; \mathbf{o}) - \mathbf{E}(\mathbf{s}; \mathbf{o})\| d\Omega \\ &< \frac{\varepsilon}{2} + \frac{\varepsilon}{2} = \varepsilon \text{ for all } \mathbf{s} \in B(\mathbf{r}, \delta_\nu), \end{aligned} \tag{30}$$

which proves continuity.

3.4. Magnetic field components

Let's fix $\mathbf{o} \in \Omega$ and consider a point \mathbf{r} with a non-zero local coordinate z . Then we can take a curl of $\mathbf{E}(\mathbf{r}; \mathbf{o}) = E_0(E_1\mathbf{e}_1 + E_3\mathbf{e}_3)$ at \mathbf{r} . As well known, a magnetic field at \mathbf{r} is

$$\mathbf{H}(\mathbf{r}; \mathbf{o}) = \frac{i}{\omega\mu} [\nabla \times \mathbf{E}(\mathbf{r}; \mathbf{o})] = \frac{i}{\omega\mu} E_0 \begin{vmatrix} \mathbf{e}_1 & \mathbf{e}_2 & \mathbf{e}_3 \\ \frac{\partial}{\partial x} & \frac{\partial}{\partial y} & \frac{\partial}{\partial z} \\ E_1 & 0 & E_3 \end{vmatrix} = E_0(H_1\mathbf{e}_1 + H_2\mathbf{e}_2 + H_3\mathbf{e}_3), \tag{31}$$

and

$$H_1 = \frac{i}{\omega\mu} \frac{\partial E_3}{\partial y}, \quad H_2 = \frac{i}{\omega\mu} \left(\frac{-\partial E_3}{\partial x} + \frac{\partial E_1}{\partial z} \right) \text{ and } H_3 = -\frac{i}{\omega\mu} \frac{\partial E_1}{\partial y}. \tag{32}$$

If AS(\mathbf{r}) is valid, we obtain a total magnetic field at \mathbf{r} as

$$\begin{aligned} \mathbf{H}(\mathbf{r}) &= \iint_{\Omega} E_0(\mathbf{o}) \left[H_1(\mathbf{r}; \mathbf{o})\mathbf{e}_1(\mathbf{o}) + H_2(\mathbf{r}; \mathbf{o})\mathbf{e}_2(\mathbf{o}) \right. \\ &\quad \left. + H_3(\mathbf{r}; \mathbf{o})\mathbf{e}_3(\mathbf{o}) \right] d\Omega. \end{aligned} \tag{33}$$

Lemma 3.4. Let Ω be a regular, compact surface in \mathbb{R}^3 , especially $\frac{\partial \mathbf{o}}{\partial p} \times \frac{\partial \mathbf{o}}{\partial q} \neq \mathbf{0}$ for all $\mathbf{o} \in \Omega$. There exist $\lim_{z \rightarrow 0^+} \mathbf{H}(\mathbf{r}; \mathbf{o})$ and $\lim_{z \rightarrow 0^-} \mathbf{H}(\mathbf{r}; \mathbf{o}) = -\lim_{z \rightarrow 0^+} \mathbf{H}(\mathbf{r}; \mathbf{o})$ at $(\mathbf{r}, \mathbf{o}) \in (\mathbb{R}^3 \setminus \Omega) \times \Omega_0(\mathbf{r})$. The function $\mathbf{H}(\mathbf{r}; \mathbf{0})$ extended by the former limit depends continuously on (\mathbf{r}, \mathbf{o}) in the set $(\mathbb{R}^3 \setminus \Omega) \times \Omega_+(\mathbf{r})$. Correspondingly, $\mathbf{H}(\mathbf{r}; \mathbf{0})$ extended by the latter limit depends continuously on (\mathbf{r}, \mathbf{o}) in $(\mathbb{R}^3 \setminus \Omega) \times \Omega_-(\mathbf{r})$.

Proof. We can follow the steps in Lemma 3.1 with a few adaptations. It is briefly seen, that $\frac{\partial^{m+n}}{\partial x^m \partial y^n} D \rightarrow 0$ for all $m + n = 1, 2, 3, \dots$, when $z \rightarrow 0$ and $s = \sqrt{x^2 + y^2} \neq 0$. It is straightforward to show that the function $\left[\frac{\partial^n}{\partial r^n} h(r; |z|) \right] r^n$ is a bounded on $r \in [k, \infty[$ for $n = 1, 2$. Actually, that holds for all $n = 1, 2, 3, \dots$

As a consequence, we obtain as in Lemma 3.1

$$\frac{\partial^{m+n}}{\partial y^m \partial x^n} E_1 \rightarrow 0 \text{ for } m + n = 1, 2, \text{ when } z \rightarrow 0. \tag{34}$$

Thus $\frac{\partial}{\partial z} H_1 = a \frac{\partial}{\partial y} \frac{\partial}{\partial z} E_3 = -a \frac{\partial}{\partial y} (ik_x E_1) = -a \frac{\partial^2}{\partial y \partial x} E_1 \rightarrow 0$, when $z \rightarrow 0$. Hence, similar to Lemma 3.1, we can conclude that there exists $\lim_{z \rightarrow 0^+} H_1$ and $\lim_{z \rightarrow 0^-} H_1 = -\lim_{z \rightarrow 0^+} H_1$.

Denote $F = -\frac{\partial}{\partial x} E_3$ and $G = \frac{\partial}{\partial z} E_1$. Then $\frac{\partial F}{\partial z} = \frac{\partial^2}{\partial x^2} E_1 \rightarrow 0$, when $z \rightarrow 0$. Hence there exist $\lim_{z \rightarrow 0^+} F$ and $\lim_{z \rightarrow 0^-} F = -\lim_{z \rightarrow 0^+} F$. The function E_1 satisfies the Helmholtz equation, so we get $\frac{\partial G}{\partial z} = \frac{\partial^2}{\partial z^2} E_1 = -(\frac{\partial^2}{\partial x^2} + \frac{\partial^2}{\partial y^2} + k^2)E_1 \rightarrow 0$, when $z \rightarrow 0$. Hence there exists $\lim_{z \rightarrow 0^+} G$ and $\lim_{z \rightarrow 0^-} G = -\lim_{z \rightarrow 0^+} G$. As a consequence we conclude that there exists $\lim_{z \rightarrow 0^+} H_2$ and $\lim_{z \rightarrow 0^-} H_2 = -\lim_{z \rightarrow 0^+} H_2$.

Moreover, $H_3 = -a \frac{\partial}{\partial y} E_1 \rightarrow 0$, when $z \rightarrow 0$, which is consistent with Lemmas 3.1 and 3.2 and the fact that $\mathbf{H} \cdot \mathbf{E} = 0$.

3.5. Theorem for the magnetic field

Theorem 3.5. Let Ω be a regular, compact surface in \mathbb{R}^3 , especially $\frac{\partial \mathbf{o}}{\partial p} \times \frac{\partial \mathbf{o}}{\partial q} \neq \mathbf{0}$ for all $\mathbf{o} \in \Omega$. The electric field E_0 on Ω creates a magnetic field $\mathbf{H}(\mathbf{r})$ at the point $\mathbf{r} \in \mathbb{R}^3 \setminus \Omega$, where the set $\Omega_0(\mathbf{r})$ is of measure zero in $d\Omega$. Moreover, $\mathbf{H}(\mathbf{r})$ is a continuous function of \mathbf{r} at those points.

Proof. We follow the proof in 3.3, where $\mathbf{E}(\mathbf{r})$ is replaced with $\mathbf{h}(\mathbf{r})$.

3.6. Note for the total field

From a physical point of view, in the article [11–13], the fields $\mathbf{E}(\mathbf{r})$ and $\mathbf{H}(\mathbf{r})$ are limits obtained by using polyhedral and the planar theory on their faces

$$\mathbf{E}(\mathbf{r}) = \lim_{|\Omega_t| \rightarrow 0} \sum_t \mathbf{E}_t(\mathbf{r}) \text{ and } \mathbf{H}(\mathbf{r}) = \lim_{|\Omega_t| \rightarrow 0} \sum_t \mathbf{H}_t(\mathbf{r}), \quad (35)$$

which are used in the torus surface field example in section 4.

4. Fields at the source surface

Some applications require computing radiated fields very near or on the source surface Ω , which, in its current form, is singular. This singularity problem can be avoided with two approaches. The first option is to restrict the integration limit of source points to finite values. Simulations have shown that integrating within a limit $1.2k$ gives accurate results without losing information or encountering singularities. The second option is to change the integration order, which allows the integration of the source points over infinite space. The change in integration order offers an approach to analyzing electromagnetic beams near and at the source surfaces. As an example, the \mathbf{E} would be computed as

$$\begin{aligned} \mathbf{E}(\mathbf{r}) &= \iint_{\Omega} E_0(\mathbf{o}) \left[E_1(\mathbf{r}; \mathbf{o}) \mathbf{e}_1(\mathbf{o}) + E_3(\mathbf{r}; \mathbf{o}) \mathbf{e}_3(\mathbf{o}) \right] d\Omega, \\ &= \iint_{\mathbb{R}^2} dk_x dk_y \iint_{\Omega} e^{i[k_x \bar{x}(\mathbf{r}; \mathbf{o}) + k_y \bar{y}(\mathbf{r}; \mathbf{o}) + k_z \bar{z}(\mathbf{r}; \mathbf{o})]} \\ &\quad * E_0(\mathbf{o}) \left[\mathbf{e}_1(\mathbf{o}) - \frac{k_x}{k_z} \mathbf{e}_3(\mathbf{o}) \right] d\Omega \end{aligned} \quad (36)$$

where $\mathbf{r} = x\mathbf{e}_x + y\mathbf{e}_y + z\mathbf{e}_z$, $\mathbf{o} = o_x\mathbf{e}_x + o_y\mathbf{e}_y + o_z\mathbf{e}_z$, $[\bar{x}(\mathbf{r}; \mathbf{o}) \ \bar{y}(\mathbf{r}; \mathbf{o}) \ \bar{z}(\mathbf{r}; \mathbf{o})]^T = \Theta^T(\mathbf{r} - \mathbf{o})$ and $\Theta = [\mathbf{e}_1(\mathbf{o}) \ \mathbf{e}_2(\mathbf{o}) \ \mathbf{e}_3(\mathbf{o})]$ is a transformation matrix introduced in [11]. This procedure is also valid for the magnetic field.

5. Beam synthesis from torus surface field

This section presents the simulation results for a large torus surface field, in which electromagnetic radiation would not be valid at any point in $\mathbf{r} \in \mathbb{R}^3 \setminus \Omega$ without the proofs of Section 3. The geometry of the torus surface is presented in Fig. 4 and MATLAB code for parametrization can be obtained from [17].

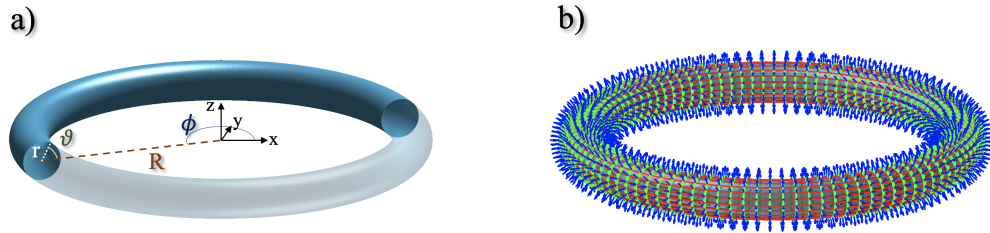


Fig. 4. a) Torus parameters. b) The torus surface is discretized to the source points, whose local base vectors ($\mathbf{e}_1, \mathbf{e}_2, \mathbf{e}_3$) are marked as red, green, and blue arrows, respectively.

The torus dimensions were selected to be significant compared to the wavelength λ , with a circumference of 30λ . This leads to a torus radius of $R = 30\lambda/2\pi$, and the torus thickness was selected $r = 0.05\lambda$. The torus surface was discretized with 1800 source points, which gives well below $\lambda/6$ spacing. In this simulation example, we synthesized an electromagnetic beam from an electric field on a torus surface, which will radiate only towards free space. Due to this, we restrict to the set $\Omega_+(\mathbf{r})$, that is, source points having local $z \geq 0$ related to \mathbf{o} . Also, it is important to note that in the following CBIM simulations, each source point radiating from the torus surface to $\Omega_+(\mathbf{r})$ direction doesn't interact with the torus structure.

5.1. Near-field radiation

The electromagnetic near-field radiation is synthesized from a torus surface field $E_0 = 1$ V/m, which is distributed as

$$j\mathbf{e}_\theta = \sigma E_0 e^{-ik\theta R} \mathbf{e}_\theta, \quad (37)$$

where surface current is $j = 1$ A/m², conductivity is $\sigma = 1$ S/m and $k = 2\pi/\lambda$ is the wavenumber. Both electric and magnetic fields are illustrated on an evaluation (x, z) -plane of a size of $4R \times 4R$, see Figs. 5 and 6. The fields are computed from 1800 source points to 500×500 evaluation points, taking approximately 4 hours to simulate on a modern laptop. As seen from the figures, the propagating electric field has destructive interference at $(x, y) = (0, 0)$ line, whereas the magnetic field has constructive interference. This near-field radiation is well aligned with the vector field geometry.

5.2. Far-field radiation

The beam synthesis from a source field positioned on the torus surface can also be interpreted as a very large loop antenna radiation with a diameter of $D \approx 9.5\lambda$ [18]. The radiation patterns of this large loop antenna cannot be computed with closed-form equations [18,19]. For this reason, we have compared the far-field radiation calculated with the CBIM to that obtained from the CST Studio Suite simulations. As the loop antenna needs a feed port(s), the surface current distribution will differ from the ideal one presented in Eq. (37). Due to this, the simulation is first done with CST Studio to obtain the far-field pattern as well as the actual surface current distribution on the torus surface, see Fig. 7.

We used four voltage ports to create a similar current distribution as in Eq. (37). Thus, we prefer to call this a torus far-field simulation rather than a loop antenna simulation. Then, the far-field radiation is simulated with CBIM using CST mesh and surface current data. Each center position on the CST mesh is replaced by a source point, in which the complex amplitude is obtained from the CST surface current data \mathbf{k}^{CST} as

$$E_0(\mathbf{o}) = \mathbf{e}_1(\mathbf{o}) \cdot \text{RE} \{ [k_x^{CST} \ k_y^{CST} \ k_z^{CST}] (\mathbf{o}) \} + i\mathbf{e}_1(\mathbf{o}) \cdot \text{IM} \{ [k_x^{CST} \ k_y^{CST} \ k_z^{CST}] (\mathbf{o}) \}. \quad (38)$$

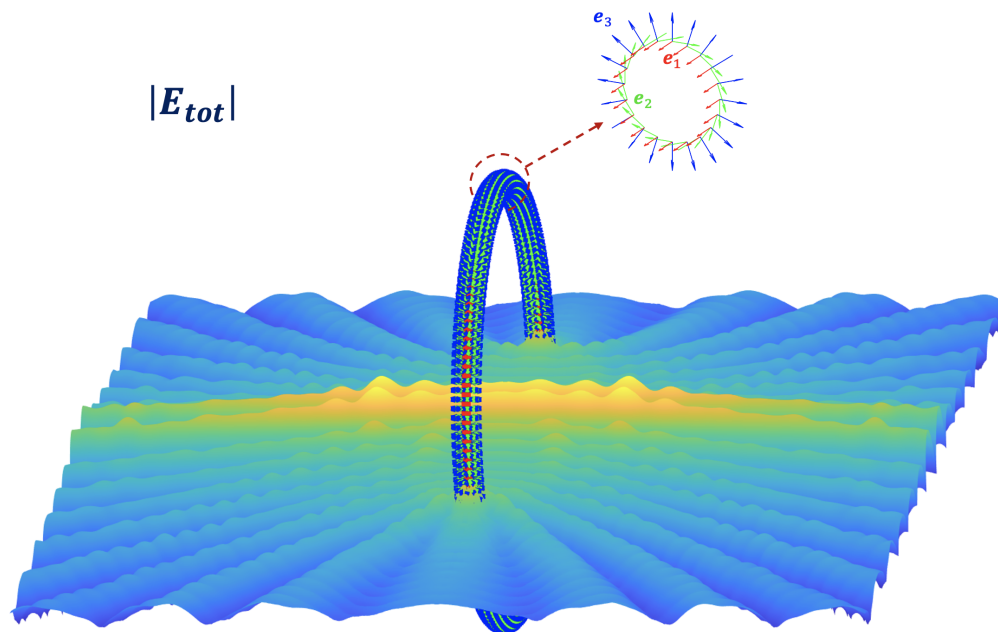


Fig. 5. The radiated electric field from a torus surface field evaluated at (x, z) -plane.

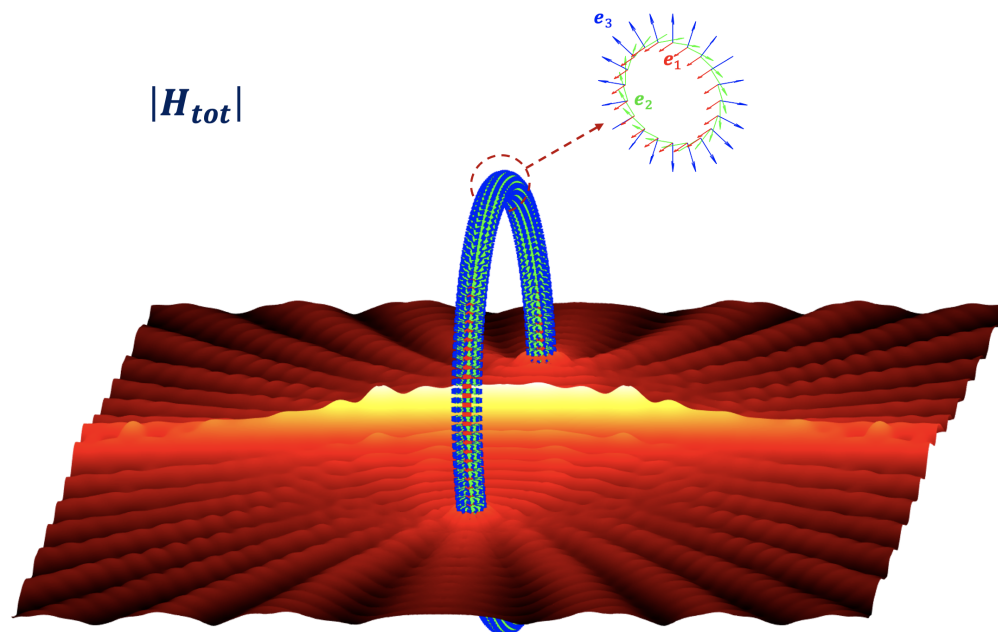


Fig. 6. The radiated magnetic field from a torus surface field evaluated at (x, z) -plane.

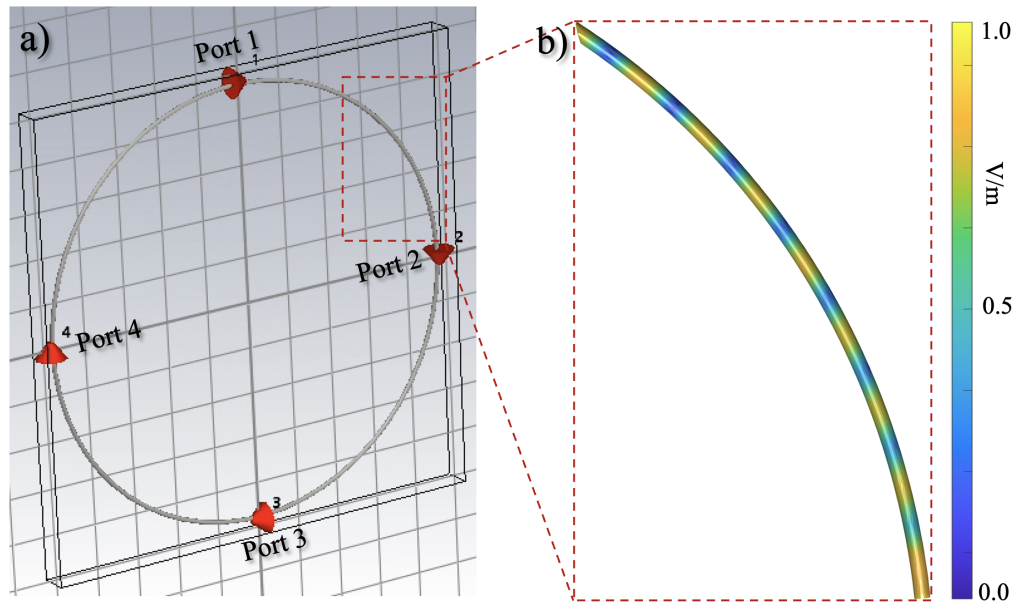


Fig. 7. a) Simulation model of the torus in CST with 4 ports and PEC material and b) an illustration of the surface current distribution.

The CBIM simulations are evaluated at a distance of $200R$ from the origin of the torus, which is well beyond the far-field distance $2D^2/\lambda$. The fields are computed from 11564 source points to 500 evaluation points, taking approximately 30 minutes to simulate on a modern laptop. The far-field electric and magnetic field cuts at (x, z) -plane simulated with CBIM and CST Studio are presented in Fig. 8. As seen from the simulation comparison, the far-field patterns are well matched for $\theta \leq |\pm 55^\circ|$. The mismatch with larger angles $\theta \geq |\pm 55^\circ|$ is due to the CBIM simulations not taking into account shadowing and scattering by the torus PEC structure as the CST electromagnetic solver did. This becomes evident when the radiation angle is large enough to intersect with the torus structure.

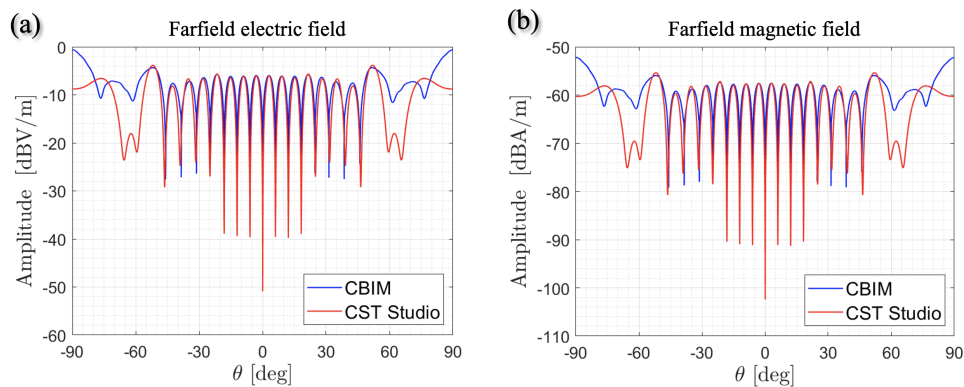


Fig. 8. The electric and magnetic far-field radiation patterns comparison to CST Studio Suite simulations. Fields are simulated on a hemisphere intersecting (x, z) -plane, where global spherical coordinates $\phi = 0$ and $\theta = [-\pi/2, \pi/2]$.

Also, the shape of electric and magnetic far-field patterns are nearly identical as the reactive near-field radiation fades away. This serves as a good example of how CBIM can simulate both near- and far-field with high accuracy.

6. Conclusions

This article addresses the limitations in the original integral presentation of the CBIM [11] for electromagnetic beams synthesized from arbitrary surface field distributions on compact surfaces Ω in \mathbb{R}^3 space. Previously, the representation was restricted to points $\mathbf{r} \in \mathbb{R}^3$ satisfying the assumption AS(\mathbf{r}) in Eq. (5). This limitation can lead to significant restriction for $\mathbf{E}(\mathbf{r})$ and $\mathbf{H}(\mathbf{r})$ synthesis due to the shape of the surface Ω . By removing this restriction, we have extended the validity of the integral representation to all points in $\mathbb{R}^3 \setminus \Omega$, where $\Omega_0(\mathbf{r})$ is of measure zero in $d\Omega$. For example, for torus surfaces Ω presented in Figs. 2 and 4, that is the case for all $\mathbf{r} \in \mathbb{R}^3 \setminus \Omega$, since $\Omega_0(\mathbf{r})$ is certainly such a set. Further, we showed that by changing the order of integrations, the integral presentation is valid on the surface Ω without singularities.

The fact that $\mathbf{E}(\mathbf{r}; \mathbf{o})$ and $\mathbf{H}(\mathbf{r}; \mathbf{o})$ are defined as limit values at some point \mathbf{o} in the generalized solution, does not play any role in the practical solution. This is because $\mathbf{E}(\mathbf{r}; \mathbf{o})$ and $\mathbf{H}(\mathbf{r}; \mathbf{o})$ are density functions in the integrals in Eq. (4) and Eq. (33), that are bounded and continuous in pieces.

We provide near-field simulation examples and prove the accuracy of the far-field radiation patterns by comparing CBIM and CST Studio Suite simulations. The far-field patterns between CBIM and CST studio simulations have a high agreement when the shadowing and scattering from torus PEC structure don't play a significant role, as the CBIM doesn't take this into account.

Our results have significant implications for electromagnetic wave theory and its practical applications, such as synthesizing and analyzing electromagnetic beams from and between shaped objects. The extended integral representation provides a more comprehensive and accurate description of beam synthesis by removing the restriction from the radiated electromagnetic beams. This flexibility allows for more precise and versatile beam design, which can be particularly useful in various electromagnetic applications.

Funding. CorneaSense; Business Finland (7383/31/2023); Assessment of the Graft Rejection Using Millimeter Waves; Research Council of Finland (327640).

Disclosures. The authors declare no conflicts of interest.

Data availability. Data underlying the results presented in this paper are available in Ref. [17].

References

1. C. B. Top, "A generalized split-step angular spectrum method for efficient simulation of wave propagation in heterogeneous media," *IEEE Trans. Ultrason., Ferroelect., Freq. Contr.* **68**(8), 2687–2696 (2021).
2. D. Pi, J. Liu, and Y. Wang, "Optimized iterative algorithm to generate computer-generated holograms based on the intermediate angular-spectrum method," *IEEE Photonics J.* **14**(3), 1–5 (2022).
3. P. Fu, D. Zhu, and F. Hu, "A near-field imaging algorithm based on angular spectrum theory for synthetic aperture interferometric radiometer," *IEEE Trans. Microwave Theory Tech.* **70**(7), 3606–3616 (2022).
4. J. Zhao, "Fast numerical propagation in high-na imaging using the resampling angular spectrum method," *Opt. Express* **30**(23), 41492–41507 (2022).
5. T. Kozacki and K. Falaggis, "Angular spectrum method with compact space-bandwidth: generalization and full-field accuracy," *Appl. Opt.* **55**(19), 5014–5024 (2016).
6. X. Yu, T. Xiahui, and Q. Y. xiong, "Wide-window angular spectrum method for diffraction propagation in far and near field," *Opt. Lett.* **37**(23), 4943–4945 (2012).
7. W. Zhao, C. Wei, and C. Yuan, "A flexible numerical calculation method of angular spectrum based on matrix product," *Opt. Lett.* **45**(21), 5937–5940 (2020).
8. K. Matsushima and T. Shimobaba, "Band-limited angular spectrum method for numerical simulation of free-space propagation in far and near fields," *Opt. Express* **17**(22), 19662–19673 (2009).
9. A. Ritter, "Modified shifted angular spectrum method for numerical propagation at reduced spatial sampling rates," *Opt. Express* **22**(21), 26265–26276 (2014).
10. T. Shimobaba, K. Matsushima, and T. Kakue, "Scaled angular spectrum method," *Opt. Lett.* **37**(19), 4128–4130 (2012).

11. J. Lamberg, F. Zarrinkhat, and A. Tamminen, "Curved boundary integral method for electromagnetic fields," *Opt. Express* **31**(26), 43583–43599 (2023).
12. J. Lamberg, F. Zarrinkhat, and A. Tamminen, "Mie scattering with 3d angular spectrum method," *Opt. Express* **31**(23), 38653–38665 (2023).
13. J. Lamberg, F. Zarrinkhat, and A. Tamminen, "Wavefront-modified vector beams for thz cornea spectroscopy," *Opt. Express* **31**(24), 40293–40307 (2023).
14. J. A. Ratcliffe, "Some aspects of diffraction theory and their application to the ionosphere," *Rep. Prog. Phys.* **19**(1), 306188 (1956).
15. E. M. Stein and G. Weiss, *Introduction to Fourier Analysis on Euclidean Spaces (PMS-32), Volume 32* (Princeton University Press, Princeton, 1972).
16. F. Maass, P. Martin, and J. Olivares, "Analytic approximation to bessel function $j_0(x)$," *Comp. Appl. Math.* **39**(3), 222 (2020).
17. J. Lambert, "MATLAB codes for Curved Boundary Integral Method," GitHub (2024), <https://github.com/Lamberg85/CBIM>.
18. R. Li, N. Bushyager, J. Laskar, *et al.*, "Determination of reactance loading for circularly polarized circular loop antennas with a uniform traveling-wave current distribution," *IEEE Trans. Antennas Propag.* **53**(12), 3920–3929 (2005).
19. R. King, "The linear antenna—eighty years of progress," *Proc. IEEE* **55**(1), 2–16 (1967).